# Fluidization of spherical versus elongated particles
## Experimental investigation using magnetic particle tracking

Mema, Ivan; Buist, Kay A.; Kuipers, J. A.M.; Padding, Johan T.

**DOI**
10.1002/aic.16895

**Publication date**
2020

**Document Version**
Final published version

**Published in**
AIChE Journal

Received: 26 September 2019 | Revised: 27 November 2019 | Accepted: 12 December 2019

DOI: 10.1002/aic.16895



# Fluidization of spherical versus elongated particles: Experimental investigation using magnetic particle tracking

Ivan Mema[1] | Kay A. Buist[2] | J.A.M. (Hans) Kuipers[2] | Johan T. Padding[1]

[1]Complex Fluid Processing, Department of Process and Energy, Delft University of Technology, Delft, Netherlands

[2]Department of Chemical Engineering and Chemistry, Multiphase Reactors Group, Eindhoven University of Technology, Eindhoven, Netherlands

**Correspondence**
Ivan Mema, Complex Fluid Processing, Department of Process and Energy, Delft University of Technology, Leeghwaterstraat 39, 2628 CB Delft, Netherlands.
Email: i.mema@tudelft.nl

## Abstract

In biomass processing fluidized beds are used to process granular materials where particles typically possess elongated shapes. However, for simplicity, in computer simulations particles are often considered spherical, even though elongated particles experience more complex particle–particle interactions as well as different hydrodynamic forces. The exact effect of these more complex interactions in dense fluidized suspensions is still not well understood. In this study we use the magnetic particle tracking technique to compare the fluidization behavior of spherical particles to that of elongated particles. We found a considerable difference between fluidization behavior of spherical versus elongated particles in the time-averaged particle velocity field as well as in the time-averaged particle rotational velocity profile. Moreover, we studied the effect of fluid velocity and the particle's aspect ratio on the particle's preferred orientation in different parts of the bed, which provides new insight in the fluidization behavior of elongated particles.

**KEYWORDS**

fluidization, elongated particles, particle orientation, particle velocity

## 1 | INTRODUCTION

Fluidized beds are encountered in many industrial applications such as gasification, drying, coating, food processing, and gas phase polymerization. In many of these processes the fluidized particles have a nonspherical shape. This is particularly the case in biomass processing which is rapidly gaining importance because of the need to switch to more sustainable energy and material sources. Biomass such as wood chips, wood pellets, and straw-like materials are characterized by an elongated shape. Elongated particles feature much more complex particle–particle interactions as well as complex hydrodynamic forces that depend on particle shape and orientation to the flow. This creates a need for better understanding of fluidization of elongated particles which explains why such systems have received considerable attention in recent years. Fluidization of elongated particles such as cylinders, ellipsoids, and spherocylinders has been the topic of several numerical investigations.[1-5] More fundamental research has also been conducted to obtain a better understanding of the hydrodynamic forces acting on individual elongated particles.[6-9]

Experimental investigations for validation of computational models for dense gas–particle flows are still quite scarce, especially for three dimenensional (3D) systems. The best established and mostly used noninvasive technique is PIV-DIA,[10] but it is limited to quasi-two dimensional systems. The first experimental research on fluidization of nonspherical particles was carried out using this technique.[1,11,12] For 3D systems, X-ray tomography (XRT) has been widely used for fluidized beds with spherical particles.[13-16] For most particle sizes, this technique can only provide insight in the bubble behavior of fluidized beds and unfortunately no information on the particle orientation, which is an important parameter for nonspherical particles. The latter requires particle tracking techniques. Recently, X-ray particle tracking velocimetry was used to investigate binary fluidized beds

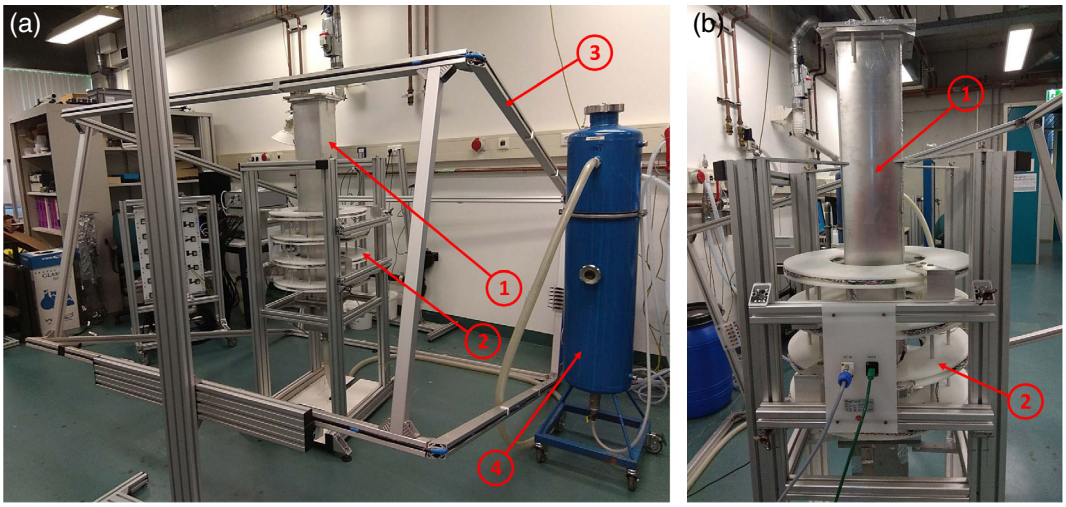


**FIGURE 1** (a) Full experimental setup, (b) close-up of the column with sensor array. 1-fluidized bed, 2-sensor array, 3-Helmholtz coil, and 4-humidifier [Color figure can be viewed at wileyonlinelibrary.com]

**TABLE 1** Dimensions and properties of the experimental setup

| *Fluidized bed* | |
|---|---|
| **Parameter** | **Value** |
| Width | 0.15 m |
| Depth | 0.15 m |
| Height | 1 m |
| Column material | Aluminum |
| *MPT sensor array* | |
| Parameter | Value |
| Sensor type | Tri-axis AMR |
| Number of sensors | 24 |
| Height | 0.45 m |
| Distance between opposing sensors | 0.26 m |
| Frequency | 1,000 Hz |

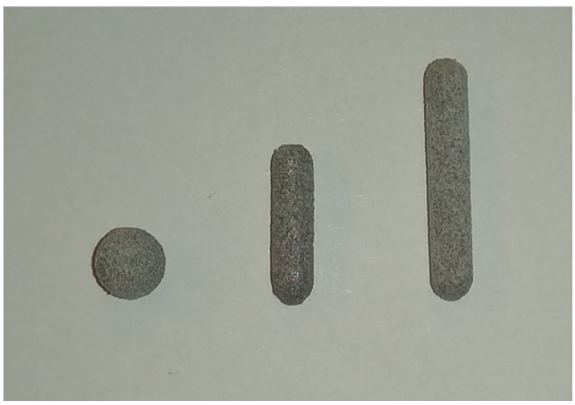

**FIGURE 2** Three dimensional printed alumide particles of aspect ratio AR-1, AR-4, and AR-6 [Color figure can be viewed at wileyonlinelibrary.com]

with cylindrical particles.[17,18] X-ray rheography is a novel technique that can be used to obtain velocity fields for 3D granular systems.[19,20] Positron emission particle tracking (PEPT) is another established particle tracking technique,[21,22] which has also been successfully used to track the orientation of nonspherical particles.[23]

The disadvantage of employing techniques like XRT and PEPT is that they require special facilities and safety measures. Therefore, the application of these techniques is challenging. Magnetic particle tracking (MPT)[24-30] has emerged as a novel experimental technique that has proven to be less expensive and safer than XRT and PEPT. MPT relies on following a magnetic dipole of a single tracer particle which allows tracking of the particle position, together with its orientation.

In this work we use the MPT technique to investigate the fluidization behavior of elongated particles. In particular, we will investigate spherocylinders of different aspect ratio, representative of biomass particles. We compare the fluidization behavior of spherocylindrical particles of two aspect ratios: aspect ratio 4 (AR-4) and aspect ratio 6 (AR-6), with that of spherical particles (AR-1), for several superficial gas velocities.

## 2 | MAGNETIC PARTICLE TRACKING

The principles behind MPT technique are thoroughly discussed in Reference 24. Here we only present a short summary. MPT is an experimental technique which relies on tracking a single magnetic marker. The magnetic tracer particle generates a quasi-static magnetic field, given by:

$$\bar{H}(\bar{u}_p,\bar{r}_{ps}) = \frac{1}{4\pi}\left(-\frac{\mu_m \bar{u}_p}{|\bar{r}_{ps}|^3} + \frac{3\mu_m(\bar{u}_p\cdot\bar{r}_{ps})\bar{r}_{ps}}{|\bar{r}_{ps}|^5}\right) \quad (1)$$

where $\bar{r}_{ps} = \bar{r}_p - \bar{r}_s$ is the relative position vector between the tracer particle and the sensor, $\mu_m$ is the magnetic moment of the tracer

**TABLE 2** Particle properties

| *Particles* | | | |
|---|---|---|---|
| **Parameter** | **AR-1** | **AR-4** | **AR-6** |
| Number of particles | 30,000 | 30,000 | 17,750 |
| Particle length (*L*) | - | 12 mm | 18 mm |
| Particle diameter (2*R*) | 5.3 mm | 3 mm | 3 mm |
| Particle material | Alumide | Alumide | Alumide |
| Particle density | 1,442 kg/m$^3$ | 1,442 kg/m$^3$ | 1,442 kg/m$^3$ |
| Mass of particle | 0.112 g | 0.112 g | 0.186 g |
| Bed height | 18 cm | 18.4 cm | 19.2 cm |
| Minimum fluidization velocity ($U_{mf}$) | 1.58 m/s | 1.7 m/s | 2.64 m/s |
| *Magnet* | | | |
| Material | N52 (NdFeB) | N52 (NdFeB) | N52 (NdFeB) |
| Length | - | 7.00 mm | 12 mm |
| Diameter | 3 mm | 1.6 mm | 1.2 mm |
| Density | 7,200 kg/m$^3$ | 7,200 kg/m$^3$ | 7,200 kg/m$^3$ |
| Magnetic moment | 0.14 Am$^2$ | 0.14 Am$^2$ | 0.14 Am$^2$ |
| *Tracer particle* | | | |
| Particle length (*L*) | - | 12 mm | 18 mm |
| Particle diameter (2*R*) | 5.30 mm | 3 mm | 3 mm |
| Particle material | Cork | European lime | European lime |
| Particle density (without magnet) | 240 kg/m$^3$ | 548 kg/m$^3$ | 548 kg/m$^3$ |
| Particle density (with magnet) | 1,796 kg/m$^3$ | 2057 kg/m$^3$ | 1,498 kg/m$^3$ |
| Mass of particle (with magnet) | 0.14 g | 0.16 g | 0.18 g |

particle, and $\bar{u}_p$ is its unit orientation vector. The magnetic field generated by the tracer particle is detected by employing multiple anisotropic magneto resistive (AMR) sensors. The tracer particle position and orientation is estimated by minimizing the difference between the theoretical and measured magnetic field strength of all sensors. The theoretical magnetic field strength is calculated for each sensor based on its position and orientation by multiplying Equation (1) with the orientation vector of the sensor

$$S_t = \bar{H}(\bar{e}_p, \bar{r}_{ps}) \cdot \bar{e}_s \tag{2}$$

Subsequently, the difference between the theoretical field strength and sensor data is minimized using Equation (3):

$$P = \frac{\sum_{i=1}^{N} erf\left(\frac{s - S_{mi}}{\sqrt{2}\sigma_i}\right)}{N} \tag{3}$$

where $N$ is the number of sensors, Sequential Quadratic Programming is used to solve the associated minimization problem.

The experimental error in determining the magnetic tracer position and orientation depends on magnetic moment of the magnet. For the tracer with a magnetic moment of 0.014 Am$^2$ used in this work, the uncertainty in determining its position and orientation is of the order of 2 mm and 2°, respectively. More information about determination of uncertainty can be found in Reference 26.

## 3 | EXPERIMENTAL SETUP

The experimental setup used in this work is shown in Figure 1. A square gas-fluidized bed is surrounded by a 3D sensor array that consists of four rings, each carrying six tri-axis AMR sensors. Setup and control are provided by Matesy GmbH. Each tri-axis sensor measures the magnetic field in 3 orthogonal directions, resulting in a total of 72 signals coming from the whole sensor array. The fluidized bed and sensor array are positioned in the center of a large Helmholtz coil to counter the effect of the earth's magnetic field. The fluidizing gas is air, the source of which is connected to a humidifier to minimize generation of static charge during fluidization. Because in these experiments we are using relatively large granular particles, not powders, using moist air for fluidization will not lead to sticking agglomerate formation. All equipment parts consist of nonmagnetizable materials. The dimensions and properties of the experimental setup are listed in Table 1.

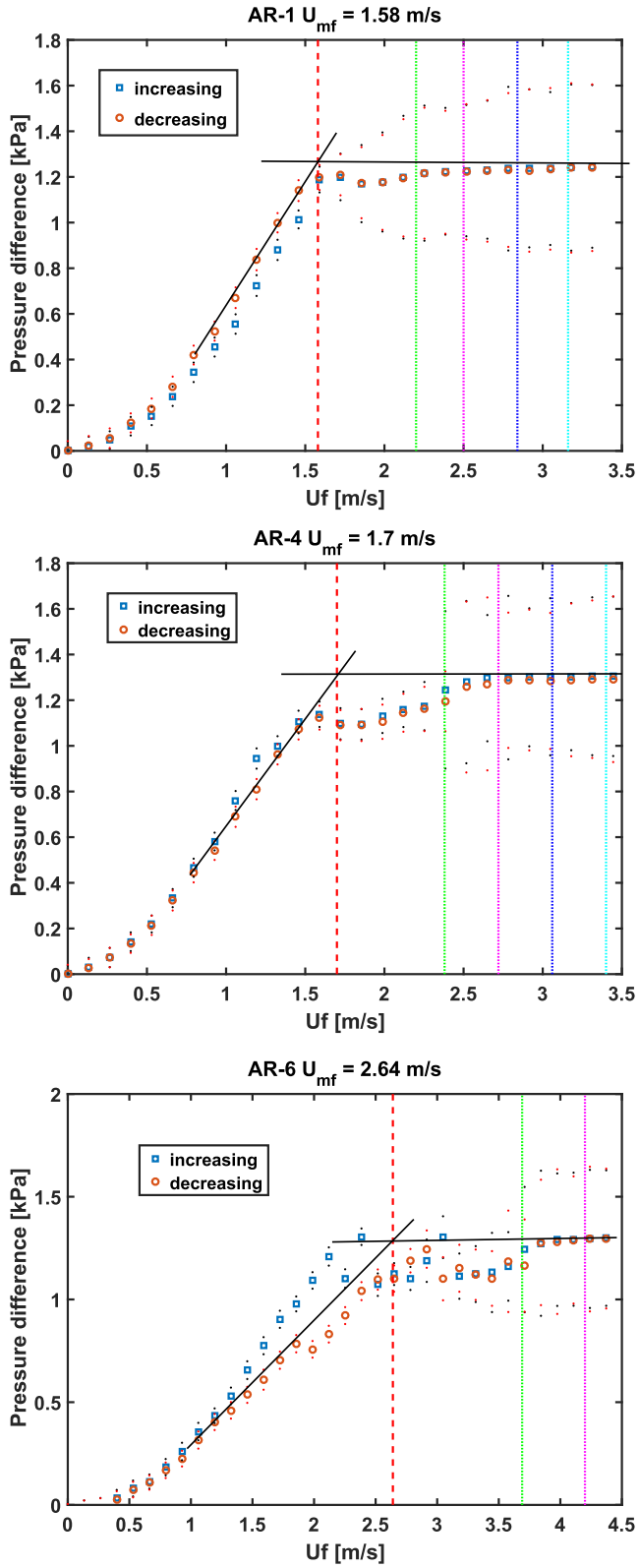


**FIGURE 3** Pressure drop measurements and minimum fluidization velocity determination for AR-1, AR-4, and AR-6 particles. The dashed red line represents the determined minimum fluidization velocity, the dotted lines indicates the used fluidization velocities: green $1.4U_{mf}$, purple $1.6U_{mf}$, blue $1.8U_{mf}$, and cyan $2U_{mf}$ [Color figure can be viewed at wileyonlinelibrary.com]

In this study three types of particles are investigated, with different aspect ratios (L/D = 1, 4, and 6), shown in Figure 2. Particles of aspect ratio 1 (AR-1) and 4 (AR-4) are volume equivalent to each other, while particles with aspect ratio 6 (AR-6) have the same diameter as AR-4 but differ in length. The minimum diameter of the particles is limited by the need to insert a magnet inside the tracer particle. The particles are 3D printed and made of alumide, a 3D printing material consisting of nylon filled with aluminum dust. The advantage of using this material (over more commonly used plastics) is that it allows, through particle contacts, for electrically conductive paths to the aluminum bed walls, thus preventing slow buildup of static charge during the experiments. In all experiments the mass of the bed is kept the same at 3.3 kg. For this mass of the bed, the initial bed heights for our particles are 17.5, 17.9, and 18.5 cm for AR-1, AR-4, and AR-6 particles, respectively. Tracer particles for aspect ratios 4 and 6 are made of European lime wood, with a density of 548 kg/m$^3$, and have the same shape and size as the bulk particles. The wooden particle is drilled along its long axis and in the middle of the particle a cylindrical neodymium magnet is inserted. The spherical tracer particle is made in a similar way: a cork sphere with a density of 240 kg/m$^3$ and 5.3 mm diameter is drilled from side to side and in the middle a spherical magnet with 3 mm diameter is positioned. The drilled holes are closed and filled with silicone. Inserting a magnet inside the tracer particle will change its moment of inertia which has to be taken into account when the presented results are used for validation of numerical models. The dimension and properties of the particles, tracer particles, and magnets used are listed in Table 2. The overall tracer particle density closely matches the density of the bulk particles. In case of aspect ratio 6 particles, the density of the tracer particle and bulk particle is identical. However, a difference in density between the tracer particle and the bulk particles for AR-1 particles is 25% and for AR-4 particles 31%. Due to the higher density of the tracer particle, it can spend a longer time at the bottom of the column and will not be lifted as high in the freeboard region as the other particles. This difference in density does not present a problem because in dense fluidizing conditions, the tracer particle will move with the rest of the bulk particles and there will be no segregation.[24,31] The only regions where caution should be taken for interpreting the results are the freeboard region and the lower part of the bed, close to the distributor plate.

## 4 | RESULTS

In this section we present and compare the fluidization characteristics for spherocylindrical particles of three different aspect ratios (aspect ratio 1, 4, and 6). The particles of aspect ratio 1 and 4 were fluidized using four different gas velocities, at $1.4U_{mf}$, $1.6U_{mf}$, $1.8U_{mf}$, and $2U_{mf}$, while the particles of aspect ratio 6 were fluidized only at 1.4 and $1.6U_{mf}$ due to limitations of the air supply. All experiments were run for 3 hr to obtain good statistical averages. We present our results in terms of the particle velocity in the vertical (z) direction, particle orientation, and particle rotation velocity.

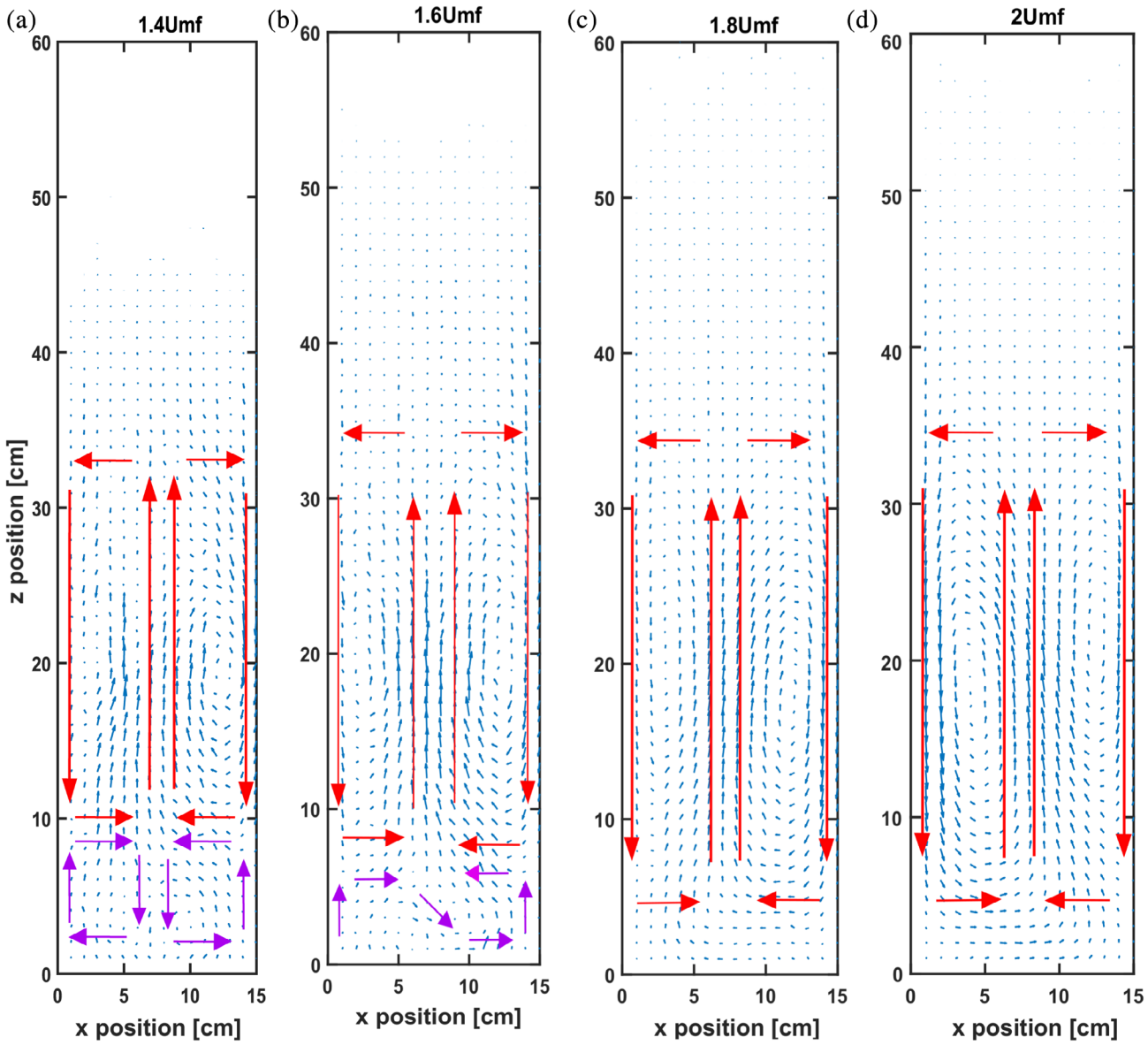


**FIGURE 4** Velocity distributions for AR-1 particles in the *x*–*z* plane for different gas inlet velocities. Positions are indicated in cm. Red and purple arrows indicate the directions of the main vortices [Color figure can be viewed at wileyonlinelibrary.com]

## 4.1 | Minimum fluidization velocity

The minimum fluidization velocity $U_{mf}$ for the particles was obtained from pressure drop measurements as described in References 1, 32 by intersection of the packed bed pressure drop line and the fluidized bed static pressure drop at decreasing flow rate. The pressure drop measurements were carried out using a MPX5050DP differential pressure sensor attached to the bottom of the column. The air flow rate was incremented in steps of 10 $nm^3$/hr, and for each value measurements were taken for 60 s at 100 Hz for both increasing and decreasing flow rate. The pressure drop curves for the three types of particles are presented in Figure 3. When determining the minimum fluidization velocity for elongated particles we need to be careful because of the additional fluidization regimes that appear in the fluidization of such particles. When fluidizing elongated particles there is no direct transition from a fixed bed to a fluidized bed, but rather there are two channeling phases (active and passive channeling), described in Reference 1, before the bed reaches the bubbling fluidizing regime. For long particles, with aspect ratio 6, the transition from a fixed bed to passive channeling is clearly noticeable in the pressure drop curve at a gas velocity of 2 m/s. The channels formed in the bed of AR-6 particles are more stable than in beds of lower aspect ratio particles, which makes it harder for them to transition to bubbling fluidization. The determined minimum fluidization velocities are listed in Table 2.

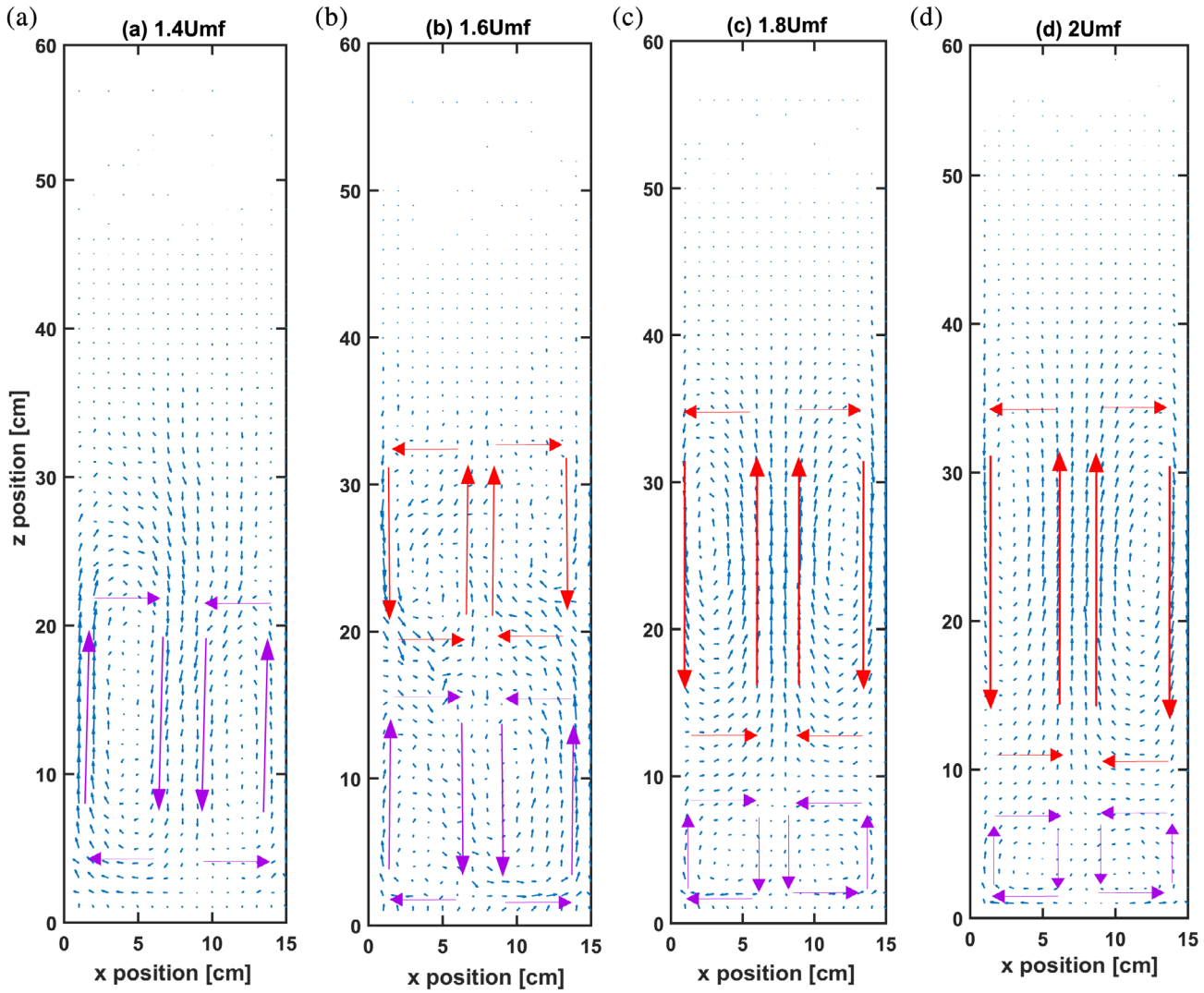


**FIGURE 5** Velocity distributions for the AR-4 particles in *x*–*z* plane for different gas inlet velocities. Positions are indicated in cm. Red and purple arrows indicate the directions of the main vortices [Color figure can be viewed at wileyonlinelibrary.com]

## 4.2 | Particle velocity

Figures 4–6 show the velocity distributions in the *x*–*z* plane for particles of aspect ratio 1, 4, and 6, respectively. The data were averaged in the *y*-direction and weighted by the number of particles in each cell of $1 \times 1$ cm used for averaging. From Figure 4 it can be seen that spherical particles tend to rise in the middle of the column and fall down next to the walls. However, at low gas inlet velocities ($1.4U_{mf}$ and $1.6U_{mf}$) two counter-rotating vortices can be noticed, one below 7 cm height, where particles rise next to the wall and move toward the center of the bed, and another one above 7 cm where particles rise in the center of the column. Increasing the gas inlet velocity reduces the size of these lower vortices until they completely disappear leaving only the upper vortex as the dominant one, which in our case for spheres can already be observed at $1.8U_{mf}$. This behavior is well-known and reported in References 32, 33, and can be explained by motion of small bubbles near the walls that tend to move away from the walls due to coalescence with neighboring bubbles. As bubble motion is the main driver of particles movement in the fluidized bed, a shift of bubble activity toward the center of the column will cause particles to rise in the middle and descend in the vicinity of the walls. With increasing gas inlet velocity, more bubbles will form above the distributor plate and their size will be larger, which leads to faster coalescence. Therefore, increasing the gas inlet velocity decreases the size of the lower vortex until it completely disappears.

Comparing the velocity profiles of spherocylindircal particles, shown in Figures 5 and 6, to the above discussed spherical particles it can be noticed that they show substantially different circulation patterns. At a low gas inlet velocity of $1.4U_{mf}$, spherocylindrical particles show only one vortex and, unlike the spheres, they rise next to the walls and descend in the middle of the column. This behavior is not discernible during the fluidization of spherical particles and agrees with the observations reported in Reference 25. An increase of gas velocity to $1.6U_{mf}$ leads to the separation of the flow and a double

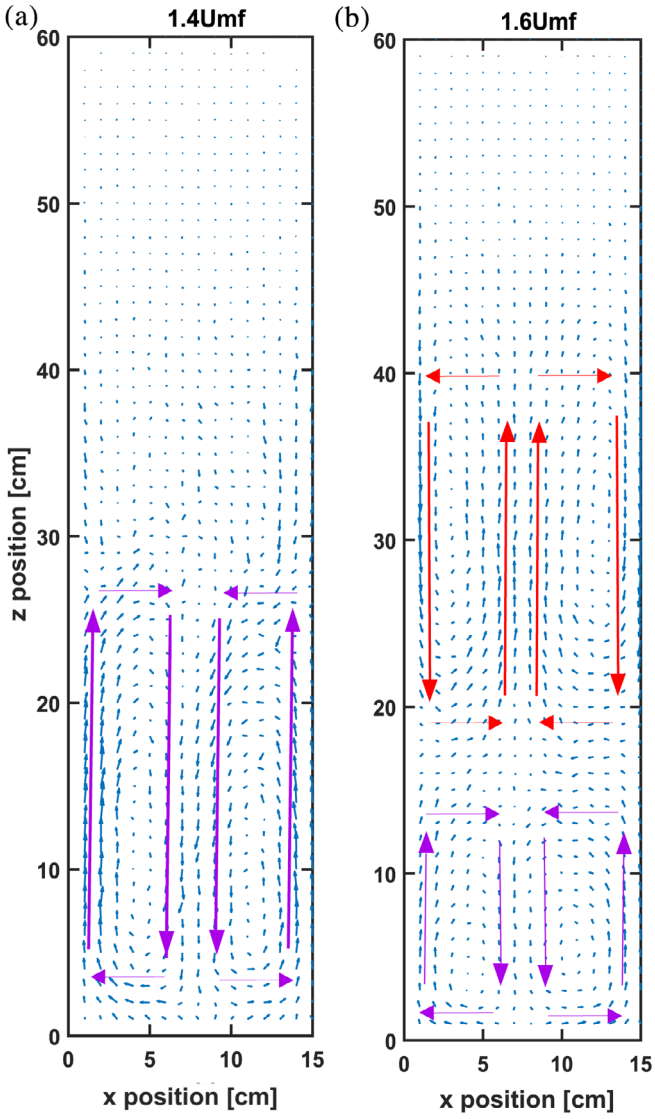


**FIGURE 6** Velocity distributions for AR-6 particles in the *x*–*z* plane for different gas inlet velocities. Positions are indicated in cm. Red and purple arrows indicate the directions of the main vortices [Color figure can be viewed at wileyonlinelibrary.com]

circulation pattern emerges such that the lower and upper vortex are roughly the same size. A further increase of the gas inlet velocity leads to a decreases of the size of the lower vortex, but it remains present even at the highest gas velocity that we considered. Spherocylindrical particles clearly show more distinct double circulation patterns, with considerably larger lower vortices than spherical particles.

The specific circulation pattern of spherocylindrical particles can be explained to be a consequence of the stronger packing of spherocylinders compared to spheres. Entanglement and higher contact surface between the particles makes it harder for bubbles to move through such a strong packing of entangled particles compared to propagation through the space between particles and walls. Therefore, at low inlet gas velocity, particles will be lifted next to the walls and descend in the middle of the column. Stronger packing also makes it harder for bubbles to coalescence and move toward the central region of the column, leading to a larger and more stable lower vortex.

## 4.3 | Particle rotational velocity

The MPT technique allows us to track the components of the rotational velocity perpendicular to the magnetic axis, which in case of our tracer particles is aligned with the particle main axis. Figures 7 and 8 show profiles of the magnitude of the particle rotational velocity in the *x*–*z* plane, averaged along the *y*-axis, for particles of aspect ratio 4 and 6, respectively. From both figures it can be observed that AR-4 and AR-6 particles have the highest rotational velocities in the free board region. From these figures it can also be seen that an increase in gas velocity leads to an increase in particle rotational velocity in the entire bed. Comparing Figures 7 and 8, it can be observed that particles with aspect ratio 6 have much higher rotational velocities than aspect ratio 4 particles.

From Figure 9 it can be seen that, unlike spherocylinders, for spherical particles, the highest rotational velocities are not encountered in the freeboard region but in the vicinity of the walls (Figure 9a,b). With increasing gas velocity, the particle rotational velocity in the bulk region of the bed also increases.

The occurrence of high rotational velocities next to the walls in case of spherical particles can be associated with rolling of particles along the wall, caused by tangential particle-wall friction. In contrast, rolling of spherocylindrical particles along the wall around an axis parallel to the wall, but perpendicular to the particles long axis is nearly impossible because of the elongated shape. There exists a possibility that spherocylinders do roll along the long particle axis, but this mode of rotation is not detectable with our current MPT system.

Even though the tracer particles have the same size and shape as the rest of the bulk particles, this is not the case for the moment of inertia, because of the inserted magnet. This needs to be taken into consideration when the presented experimental data is used to validate numerical models.

## 4.4 | Particle orientation

Unlike spherical particles, nonspherical particles can possess different orientation relative to direction of the fluid flow. This is an important characteristic of nonspherical particles, because orientation of the particles relative to the fluid flow affects the magnitude of the drag force they experience and also increases the importance of shape induced lift force and hydrodynamic torque.[2,7,8] Figure 10 shows the effect of changing the gas velocity on particle orientation relative to the *z*-axis. To avoid the effect of the slightly higher tracer density, discussed in Section 3, the free-board region and lower part of the bed, and close to the distributor plate are excluded from the averaging. We therefore focus on the bulk region between 10 and 35 cm height. For particles in a fluidized bed, the orientation with respect to the main direction of gas flow is important. Therefore, we focus on the *z*-component of the particle orientation vector $u_z$, which can provide

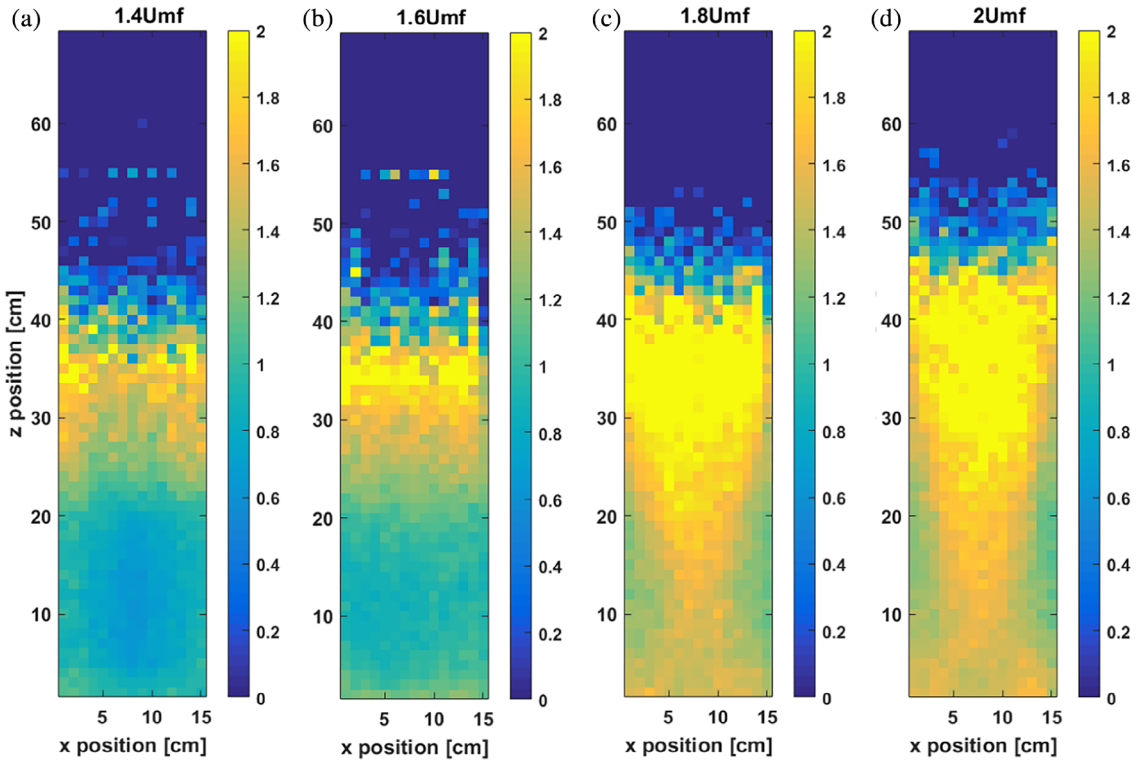


**FIGURE 7** Rotational velocity (rot/s) distributions, for rotations around axes perpendicular to the long axis of the particle, in the *x*–*z* plane for AR-4 particles [Color figure can be viewed at wileyonlinelibrary.com]

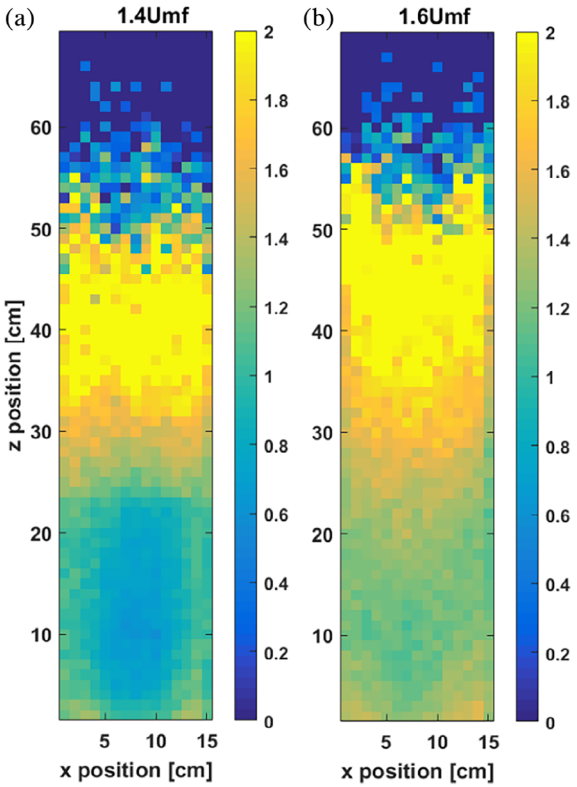


**FIGURE 8** Rotational velocity (rot/s) distributions, for rotations around axes perpendicular to the long axis of the particle, in the *x*–*z* plane for AR-6 particles [Color figure can be viewed at wileyonlinelibrary.com]

information on the particles alignment: for $u_z = \pm 1$ the particle is fully aligned with the main flow, while for $u_z = 0$ the particle is perpendicular to the main flow direction.

Figure 10 shows that with increasing gas velocity, the fraction of particles oriented vertically increases while the fraction of particles that orient horizontally decreases. At a low gas velocity of $1.4U_{mf}$ for both aspect ratio particles there exists a peak for horizontal orientation of particles, which disappears with increasing gas velocity. Figure 11 compares the *z*-orientation distribution of AR-4 and AR-6 particles at two different gas velocities. At a gas velocity of $1.4U_{mf}$ in both cases we observe a clear peak for horizontal orientation. However while the majority of AR-4 particles at this velocity tend to orient horizontally in case of AR-6 particles there is also a strong preference for vertical orientation. At a superficial velocity of $1.6U_{mf}$ in both cases an increase in fraction of particles oriented vertically can be observed but the stronger preference of AR-6 particles for vertical orientation is still evident.

While Figures 10 and 11 give insight into the average orientation of particles with respect to the *z*-axis, Figures 12 and 13 display the preferred orientation of particles in different parts of the reactor. The particle preferred orientation can be measured using the nematic tensor **S** defined as:

$$\mathbf{S} = \begin{bmatrix} \langle u_x^2 \rangle & \langle u_x u_y \rangle & \langle u_x u_z \rangle \\ \langle u_y u_x \rangle & \langle u_y^2 \rangle & \langle u_y u_z \rangle \\ \langle u_z u_x \rangle & \langle u_z u_y \rangle & \langle u_z^2 \rangle \end{bmatrix}. \quad (4)$$

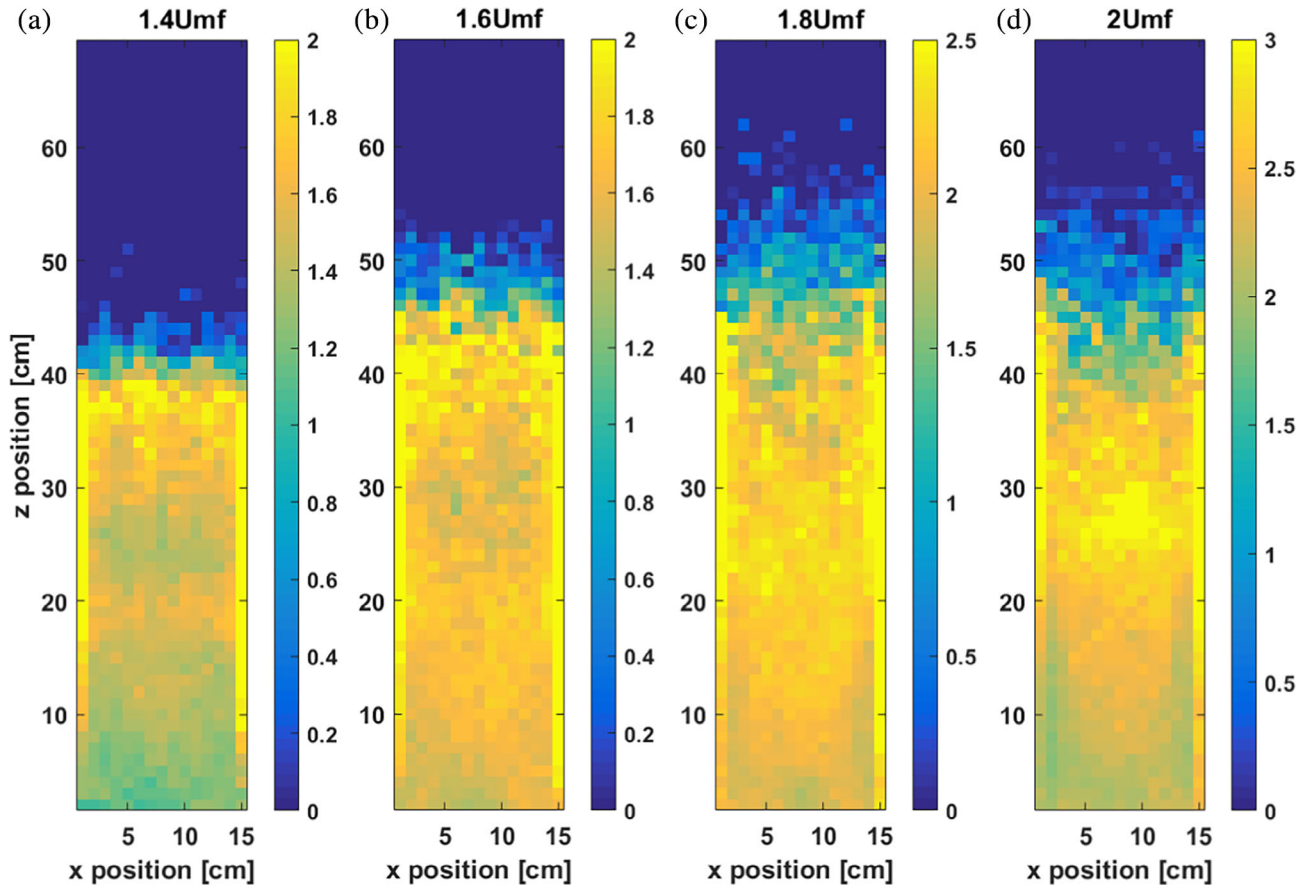


**FIGURE 9** Rotational velocity (rot/s) distributions in the *x*–*z* plane for AR-1 particles [Color figure can be viewed at wileyonlinelibrary.com]

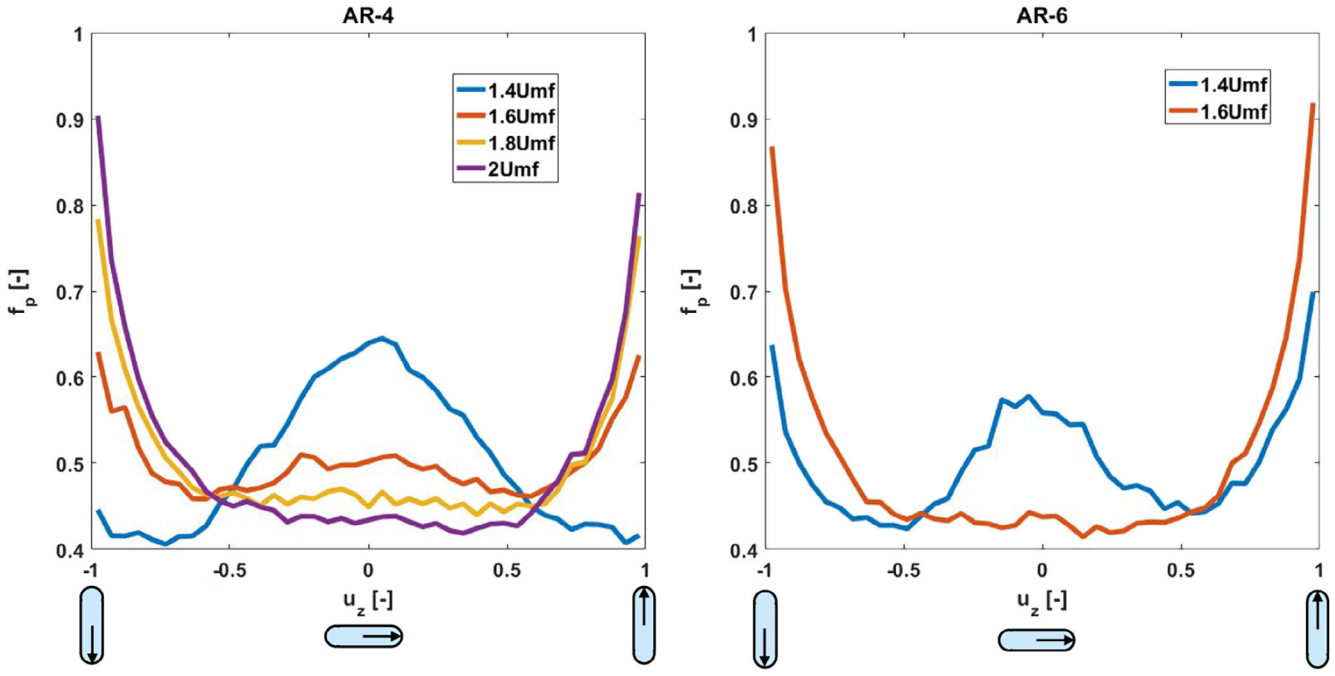


**FIGURE 10** Effect of gas velocity on the time-averaged fraction ($f_p$) of particle orientation in the *z*-direction ($u_z$) of AR-4 and AR-6 particles [Color figure can be viewed at wileyonlinelibrary.com]

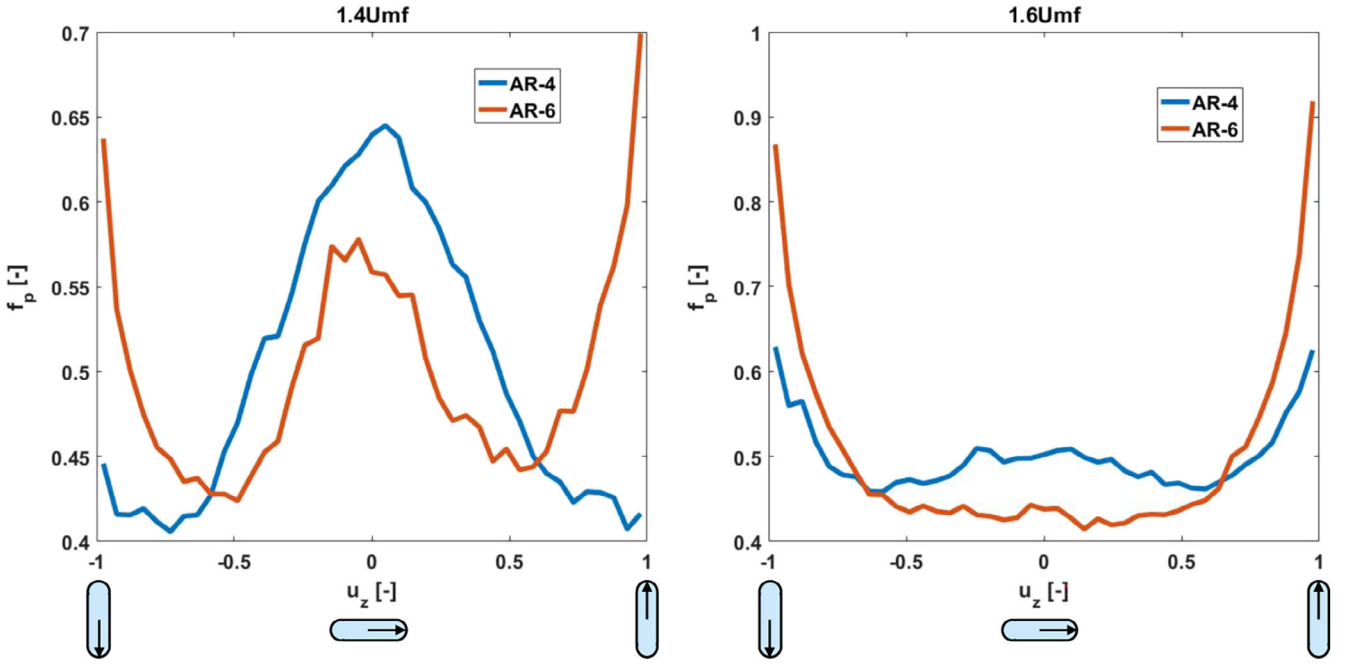


**FIGURE 11** Comparison of time-averaged particle orientation in the *z*-direction for AR-4 and AR-6 particles [Color figure can be viewed at wileyonlinelibrary.com]

Values of the diagonal components of the orientation tensor indicate preferred alignment of particles with one of the Cartesian axes. If one of the components is considerably larger than others, it can be concluded that the particle is preferably aligned with that corresponding axis. Otherwise, if the difference between the diagonal components is less than 0.1, that is, $\left|\langle u_x^2\rangle - \left\langle u_y^2\right\rangle\right| < 0.1$ , $\left|\langle u_x^2\rangle - \langle u_z^2\rangle\right| < 0.1$ , and $\left|\left\langle u_y^2\right\rangle - \langle u_z^2\rangle\right| < 0.1$, the particle is considered to be randomly oriented.

Figures 12 and 13 reveal the predominant particle alignment in different parts of the bed in the *x*–*z* plane for different inlet gas velocities. Values are temporally averaged and averaged over the *y*-direction. The coding color scheme is such that blue cells indicate preferred orientation of particles in the *x*-direction, green cells indicate preferred alignment with the *y*-direction, and red cells indicate alignment with the *z*-axis. Cyan cells indicate random orientation of the particles.

From Figure 12a it can be seen that at $1.4U_{mf}$ particles in the entire bed feature either horizontal or random orientation. In the lower part of the fluidized bed (below 10 cm), as well as in the central section and in the vicinity of the walls, particles assume a horizontal orientation such that in the middle they align with the *x*-axis but next to the walls they align with the *y*-axis. The horizontal orientation of the particles observed in the bulk region at the lowest fluidization velocity is due to the very mild fluidization at this velocity and less randomizing particle–particle collisions, therefore the features are still close to that in a nonfluidized packed bed. In the freeboard region, and in the parts between the middle section and walls, particles are randomly oriented. In Figure 12b, for $u_f = 1.6U_{mf}$, an increase in random orientation of particles can be observed. In the lower part, close to the distributor plate, particles still have a preferably horizontal alignment, as well as in the lower free-board region, between 30 and 40 cm height. The horizontal orientation of the particles in the lower free-board region is the consequence of hydrodynamic torque.[2] In this region, particles move more-or-less individually and without the perturbing influence of neighboring particles they tend to orient horizontally in a planar upward flow due to the stabilizing effect of hydrodynamic torque. Next to the walls, particles still tend to align with the *y*-axis but an increase of alignment with the *z*-axis can also be seen in that region. A further increase of the gas velocity, see Figure 12c,d, leads to an increase in vertical orientation, particularly in the middle of the dense region of the fluidized bed, between 10 and 20 cm height and next to the walls. At the same time, we notice a stronger preference in the lower freeboard region, between 30 and 40 cm height, for particles to orient horizontally.

Similar trends can be observed for AR-6 particles, as shown in Figure 13. An increase of fluid velocity reduces the tendency of particles to orient horizontally and increases the preference for vertical orientation. Comparing Figures 12 and 13a,b reveal that AR-6 particles show stronger preference to orient vertically compared to AR-4 particles. This was already concluded from Figure 11, but from Figures 12 and 13 it becomes apparent that the stronger preference of AR-6 particles to orient vertically is mostly occurring next to the walls.

## 5 | DISCUSSION AND CONCLUSION

In this work, we applied MPT to compare the fluidization behavior of spherical and elongated particles at different gas velocities. We studied three types of particles: spheres and spherocylinders with aspect

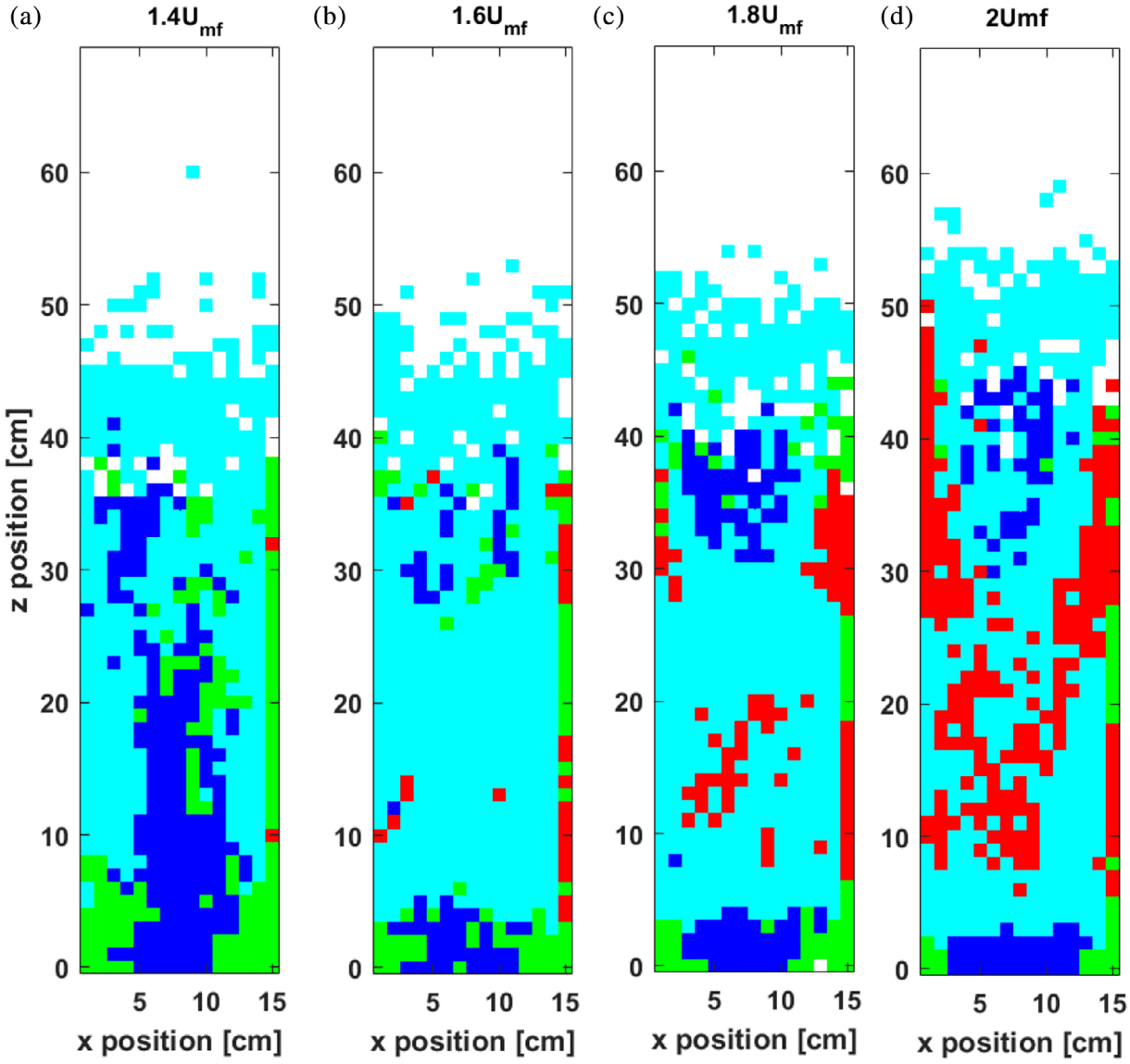


**FIGURE 12** Distribution of the predominant orientation of AR-4 particles in the *x*–*z* plane. Here the colour scheme is: blue squares (■) are *x*-aligned, green squares (■) are *y*-aligned, red squares (■) are *z*-aligned, and cyan squares (■) are randomly oriented. White space represents empty cells. Schematic representation of color scheme is shown in Figure 13 [Color figure can be viewed at wileyonlinelibrary.com]

ratio 4 and 6. The MPT technique provides us detailed insight into particles translation and rotation as well as particle orientation in a full 3D gas-fluidized bed.

Regarding the particle preferred orientation, we observed a higher tendency for AR-6 particles to align with the gas flow than AR-4 particles. This is particularly the case in the wall region where in both cases particles align to the walls but AR-6 particles are also preferably aligned with the direction of gas flow, while AR-4 particles are perpendicular to it. Using the MPT results we have also mapped out different zones in our gas-fluidized bed based on the particles preferred orientation, as shown in Figures 12 and 13. In all considered cases, the particles assume a horizontal position in the lower part of the bed, close to the distributor plate. In the wall region, particles tend to align with the walls, where at low gas velocities they are lying in a horizontal position but with increase in gas velocity they align with the flow and assume a vertical position. The bulk region of dense particle flow is defined between 10 and 20 cm height and 5 and 10 cm in the horizontal *x*-direction. In this region, at low gas velocities ($1.4U_{mf}$), the particles are oriented horizontally. An increase in gas velocity leads to randomization of particle orientations, while further increase to $1.8U_{mf}$ and $2U_{mf}$ changes the particle's preferred orientation to vertical. Generally, we observed that with increasing the gas velocity the particles preference to align with the direction of gas flow increases.

In the distribution of the particle rotational velocity, we see a clear difference between spherical and elongated particles. For a bed of spherical particles, we observe the highest rotational velocities in the bulk region and in the vicinity of the walls, while elongated

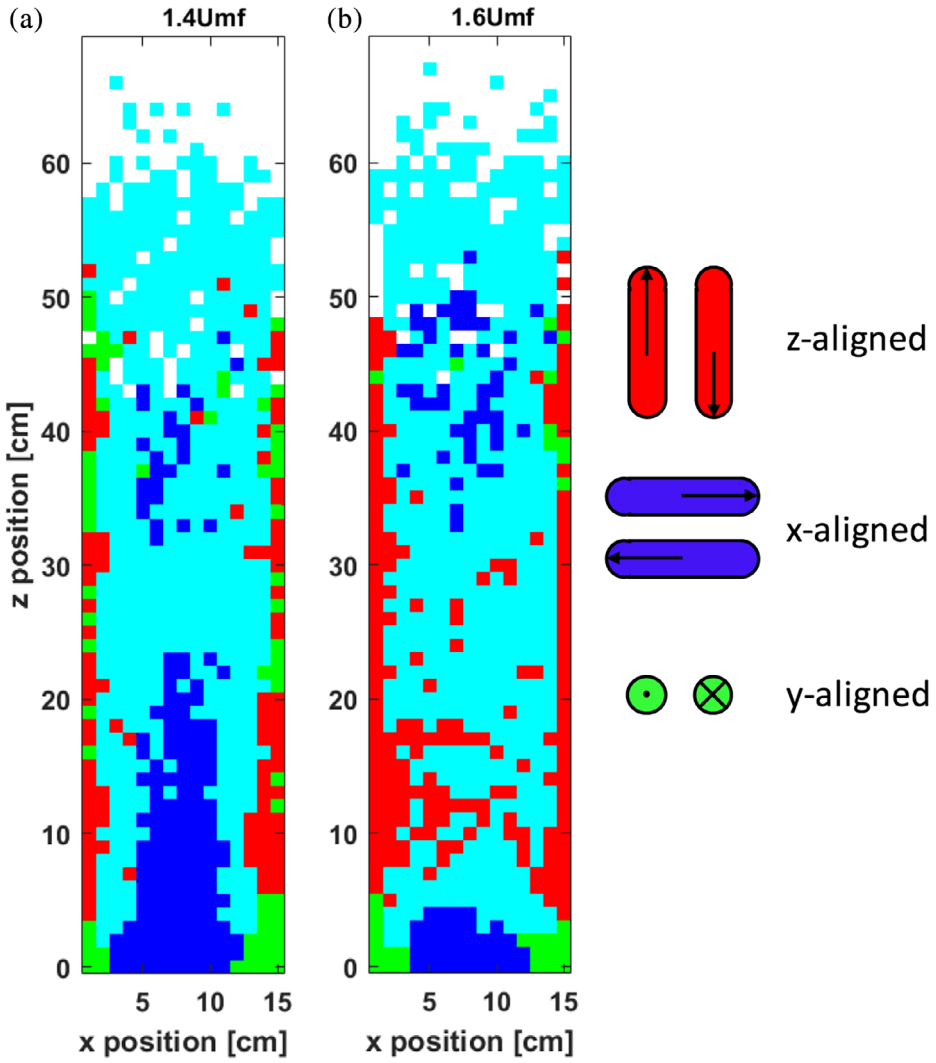


**FIGURE 13** AR-6 particle prefered orientation in *x*–*z* plane. Here the colour scheme is: blue squares (■) are *x*-aligned, green squares (■) are *y*-aligned, red squares (■) are *z*-aligned, and cyan squares (■) are randomly orientated. White space represents empty cells [Color figure can be viewed at wileyonlinelibrary.com]

particles posses the highest rotational velocities in the free-board region. These results are consistent with findings by Reference 25. Varying the particle aspect ratio also has an effect on the rotational velocity: we found that higher aspect ratio particles experience higher magnitudes of rotational velocity. As previously stated in Section 1, we have to be cautious when considering the results of particle rotation obtained from MPT, because we are only capturing one mode of rotation.

A clear difference between spherical and elongated particles is also observed in the particle velocity distributions, discussed in Section 1. For spherical particles, the velocity distribution shows that particles rise in the middle of the bed and descend next to the walls. This behavior is dominant at all gas velocities. However, in case of elongated particles we observed a completely different behavior. At low gas velocity ($1.4U_{mf}$), particles rise next to the walls and descend in the middle of the bed, a result which is not obtained for fluidization of spherical particles. For both spherical and elongated particles we encounter cases where double circulation patterns are present and flow is separated into two counter rotating vortices: a lower one where particles rise next to the walls and descend in the middle of the bed and an upper one where they are rising in the middle and descend next to the walls. For spherical particles this behavior can be noticed only at the lowest gas velocity ($1.4U_{mf}$) while it is the main characteristic of elongated particles. For AR-4 and AR-6 particles at a gas velocity of $1.6U_{mf}$, the particle velocity distribution is separated in two counter rotating vortices of the same size. Increasing the gas velocity reduces the size of the lower vortex, while the upper one where particles rise in the middle of the bed becomes the dominant one.

The considerable difference between spherical and elongated particles, reported in this work, emphasizes the need for further development of numerical models for simulation of gas-fluidized beds with elongated particles. The presented results will be valuable for future validations of simulation results. MPT is a powerful noninvasive experimental technique that can provide insight into the behavior of particles in full 3D fluidized bed. However, it also has its limitations. It can give us only time-averaged values for important fluidization parameters, therefore short lived structures, like bubbles and clusters, cannot be captured with it. As bubble properties are important characteristics of gas-fluidized beds, necessary for optimization of the

equipment, in our future work we will apply XRT analysis of the same systems to study bubbling behavior of elongated particles.

## ACKNOWLEDGMENTS

The authors thank the European Research Council for its financial support under its consolidator grant scheme, contract No.615096 (NonSphereFlow).

## ORCID

*Ivan Mema* https://orcid.org/0000-0003-2587-8613
*Kay A. Buist* https://orcid.org/0000-0003-1765-576X

## REFERENCES

1. Mahajan VV, Nijssen TMJ, Kuipers JAM, Padding JT. Non-spherical particles in a pseudo-2D fluidised bed: modelling study. *Chem Eng Sci*. 2018;192:1105-1123.
2. Mema I, Mahajan VV, Fitzgerald BW, Padding JT. Effect of lift force and hydrodynamic torque on fluidisation of non-spherical particles. *Chem Eng Sci*. 2019;195:642-656.
3. Seelen LJH, Padding Johan T, Kuipers JAM. A granular discrete element method for arbitrary convex particle shapes: method and packing generation. *Chem Eng Sci*. 2018;189:84-101.
4. Oschmann T, Vollmari K, Kruggel-Emden H, Wirtz S. Numerical investigation of the mixing of non-spherical particles in fluidized beds and during pneumatic conveying. *Procedia Eng*. 2015;102:976-985.
5. Cai J, Li Q, Yuan Z. Orientation of cylindrical particles in gas–solid circulating fluidized bed. *Particuology*. 2012;10:89-96.
6. Marian Z, George M, Fan Z, Berend W. Derivation of drag and lift force and torque coefficients for non-spherical particles in flows. *Int J Multiphase Flow*. 2012;39:227-239.
7. Sanjeevi SKP, Padding JT. On the orientational dependence of drag experienced by spheroids. *J Fluid Mech*. 2017;820:R1.
8. Sanjeevi SKP, Kuipers JAM, Padding JT. Drag, lift and torque correlations for non-spherical particles from stokes limit to high Reynolds numbers. *Int J Multiphase Flow*. 2018;106:325-337.
9. Zarghami A, Padding JT. Drag, lift and torque acting on a two-dimensional non-spherical particle near a wall. *Adv Powder Technol*. 2018;29:1507-1517.
10. Jong JF, Odu SO, Buijtenen MS, Deen NG, Sint Annaland M, Kuipers JAM. Development and validation of a novel digital image analysis method for fluidized bed particle image velocimetry. *Powder Technol*. 2012;230:193-202.
11. Vollmari K, Jasevičius R, Kruggel-Emden H. Experimental and numerical study of fluidization and pressure drop of spherical and non-spherical particles in a model scale fluidized bed. *Powder Technol*. 2016;291:506-521.
12. Boer L, Buist KA, Deen NG, Padding JT, Kuipers JAM. Experimental study on orientation and de-mixing phenomena of elongated particles in gas-fluidized beds. *Powder Technol*. 2018;329:332-344.
13. Grassler T, Wirth KE. X-ray computer tomography—potential and limitation for the measurement of local solids distribution in circulating fluidized beds. *Chem Eng J*. 2000;77:65-72.
14. Mudde RF. Time-resolved X-ray tomography of a fluidized bed. *Powder Technol*. 2010;199:55-59.
15. Xiaogang Y, Ruud OJ, Jasper S, Mudde Robert F. A hybrid tomographic reconstruction algorithm for high speed X-ray tomography. *Comput Phys Commun*. 2015;196:27-35.
16. Verma Vikrant PJT, Deen Niels G, et al. Bubble dynamics in a 3-D gas-solid fluidized bed using ultrafast electron beam X-ray tomography and two-fluid model. *AIChE J*. 2014;60:1632-1644.
17. Chen X, Zhong W, Heindel TJ. Using stereo XPTV to determine cylindrical particle distribution and velocity in a binary fluidized bed. *AIChE J*. 2018;65:520-535.
18. Chen X, Zhong W, Heindel TJ. Orientation of cylindrical particles in a fluidized bed based on stereo X-ray particle tracking velocimetry (XPTV). *Chem Eng Sci*. 2019;203:104-112.
19. Guillard F, Marks B, Einav I. Dynamic X-ray radiography reveals particle size and shape orientation fields during granular flow. *Sci Rep*. 2017;7:8155.
20. Baker J, Guillard F, Marks B, Einav I. X-ray rheography uncovers planar granular flows despite non-planar walls. *Nat Commun*. 2018;9:5119.
21. Parker DJ, Leadbeater TW, Fan X, Hausard MN, Ingram A, Yang Z. Positron imaging techniques for process engineering: recent developments at Birmingham. *Measurement Science Technol*. 2008;19:094004.
22. Link JM, Deen NG, Kuipers JAM, et al. PEPT and discrete particle simulation study of spout-fluid bed regimes. *AIChE J*. 2008;54:1189-1202.
23. Yang Z, Fan X, Bakalis S, Parker DJ, Fryer PJ. A method for characterising solids translational and rotational motions using multiple-positron emission particle tracking (multiple-PEPT). *Int J Multiphase Flow*. 2008;34:1152-1160.
24. Buist Kay A, Gaag Alex C, Deen Niels G, Kuipers Johannes AM. Improved magnetic particle tracking technique in dense gas fluidized beds. *AIChE J*. 2014;60:3133-3142.
25. Buist KA, Jayaprakash P, Kuipers JAM, Deen NG, Padding JT. Magnetic particle tracking for nonspherical particles in a cylindrical fluidized bed. *AIChE J*. 2017;63:5335-5342.
26. Yang L, Padding JT, Buist KA, Kuipers JAM. Three-dimensional fluidized beds with rough spheres: validation of a two fluid model by magnetic particle tracking and discrete particle simulations. *Chem Eng Sci*. 2017;174:238-258.
27. Richert H, Kosch O, Görnert P. Magnetic monitoring as a diagnostic method for investigating motility in the human digestive system. In: Andrä W, Nowak H, eds. *Magnetism in Medicine*. Berlin: Wiley-VCH; 2007.
28. Mohs G, Gryczka O, Heinrich S, Mörl L. Magnetic monitoring of a single particle in a prismatic spouted bed. *Chem Eng Sci*. 2009;64:4811-4825.
29. Köhler A, Rasch A, Pallarès D, Johnsson F. Experimental characterization of axial fuel mixing in fluidized beds by magnetic particle tracking. *Powder Technol*. 2017;316:492-499.
30. Tao X, Tu X, Wu H. A new development in magnetic particle tracking technology and its application in a sheared dense granular flow. *Rev Sci Inst*. 2019;90:065116.
31. Buist KA, Erdewijk TW, Deen NG, Kuipers JAM. Determination and comparison of rotational velocity in a pseudo 2-D fluidized bed using magnetic particle tracking and discrete particle modeling. *AIChE J*. 2015;61:3198-3207.
32. Kunii D, Levenspiel O. *Fluidization Engineering*, 2nd ed. Stoneham, MA (USA): Elsevier Science; 2013.
33. Laverman JA, Fan X, Ingram A, et al. Experimental study on the influence of bed material on the scaling of solids circulation patterns in 3D bubbling gas–solid fluidized beds of glass and polyethylene using positron emission particle tracking. *Powder Technol*. 2012;224:297-305.

**How to cite this article:** Mema I, Buist KA, Kuipers JAM, Padding JT. Fluidization of spherical versus elongated particles: Experimental investigation using magnetic particle tracking. *AIChE J*. 2019;e16895. https://doi.org/10.1002/aic.16895